A fabrication process for flexible single-crystal perovskite devices

https://doi.org/10.1038/s41586-020-2526-z

Received: 5 October 2019

Accepted: 22 May 2020

Published online: 29 July 2020

Check for updates

Yusheng Lei[1,9], Yimu Chen[1,9], Ruiqi Zhang[1], Yuheng Li[1], Qizhang Yan[1], Seunghyun Lee[2], Yugang Yu[3], Hsinhan Tsai[4], Woojin Choi[5], Kaiping Wang[3], Yanqi Luo[1], Yue Gu[3], Xinran Zheng[6], Chunfeng Wang[7], Chonghe Wang[1], Hongjie Hu[1], Yang Li[1], Baiyan Qi[3], Muyang Lin[1], Zhuorui Zhang[1], Shadi A. Dayeh[1,3,5], Matt Pharr[2], David P. Fenning[1], Yu-Hwa Lo[3,5], Jian Luo[1,3], Kesong Yang[1], Jinkyoung Yoo[4], Wanyi Nie[4] & Sheng Xu[1,3,5,8]✉

Organic–inorganic hybrid perovskites have electronic and optoelectronic properties that make them appealing in many device applications[1–4]. Although many approaches focus on polycrystalline materials[5–7], single-crystal hybrid perovskites show improved carrier transport and enhanced stability over their polycrystalline counterparts, due to their orientation-dependent transport behaviour[8–10] and lower defect concentrations[11,12]. However, the fabrication of single-crystal hybrid perovskites, and controlling their morphology and composition, are challenging[12]. Here we report a solution-based lithography-assisted epitaxial-growth-and-transfer method for fabricating single-crystal hybrid perovskites on arbitrary substrates, with precise control of their thickness (from about 600 nanometres to about 100 micrometres), area (continuous thin films up to about 5.5 centimetres by 5.5 centimetres), and composition gradient in the thickness direction (for example, from methylammonium lead iodide, $MAPbI_3$, to $MAPb_{0.5}Sn_{0.5}I_3$). The transferred single-crystal hybrid perovskites are of comparable quality to those directly grown on epitaxial substrates, and are mechanically flexible depending on the thickness. Lead–tin gradient alloying allows the formation of a graded electronic bandgap, which increases the carrier mobility and impedes carrier recombination. Devices based on these single-crystal hybrid perovskites show not only high stability against various degradation factors but also good performance (for example, solar cells based on lead–tin-gradient structures with an average efficiency of 18.77 per cent).

The schematic and optical images in Fig. 1a illustrate the fabrication process of single crystals using a solution-based lithography-assisted epitaxial-growth-and-transfer method. A bulk crystal of hybrid perovskites (for example, methylammonium lead iodide, $MAPbI_3$) serves as the substrate to epitaxially grow single-crystal hybrid perovskites (see Supplementary Discussion 1 and Supplementary Figs. 1–3 for more details). A 2-μm layer of patterned polymer (for example, parylene) serves as the growth mask[13,14] (Extended Data Fig. 1). The as-grown epitaxial single-crystal film can be transferred to an arbitrary substrate, maintaining a good crystallinity and a strong adhesion to the substrates (Extended Data Fig. 2; see Supplementary Discussions 1 and 2 and Supplementary Figs. 2–9 for more details). Figure 1b shows scanning electron microscope (SEM) images of an intact single-crystal $MAPbI_3$ thin film transferred onto a curved general substrate, with dimensions of about 1 cm × 1 cm × 2 μm and a monolithic cross-section without any grain boundaries that are typically seen in polycrystalline $MAPbI_3$ thin films (Fig. 1b, inset, and Supplementary Fig. 10). With a more rigid growth mask, a scaled single-crystal $MAPbI_3$ thin film with dimensions of about 5.5 cm × 5.5 cm × 20 μm can be achieved (Extended Data Fig. 3; see Supplementary Discussion 3 for more details).

A high-resolution transmission electron microscope (TEM) image further reveals the epitaxial relationship and an absence of dislocations in the as-grown $MAPbI_3$ single-crystal thin film (Fig. 1c). θ–2θ X-ray diffraction (XRD) and photoluminescence (PL) studies prove the high crystallinity of the single-crystal $MAPbI_3$ thin films fabricated by this growth-and-transfer method (Fig. 1d, e). Similar full-width at half-maximum (FWHM) of the XRD ω-scan (400) and PL peaks of the as-fabricated single-crystal $MAPbI_3$ thin films to those of the bulk single crystals indicate their comparably high crystal quality (Fig. 1d, e; see Supplementary Discussion 4 and Supplementary Fig. 11, 12 for more details). The high crystal quality is attainable over a growth temperature ranging from 80 °C to 160 °C (Fig. 1d, bottom), indicating the potential broad applicability of this growth-and-transfer method to other perovskites with different growth temperatures and crystallization conditions. Furthermore, the ratio of the PL intensity (I_{PL}) of the transferred epitaxial single-crystal thin film to the excitation intensity (I_E) shows a

[1]Department of Nanoengineering, University of California San Diego, La Jolla, CA, USA. [2]Department of Mechanical Engineering, Texas A&M University, College Station, TX, USA. [3]Material Science and Engineering Program, University of California San Diego, La Jolla, CA, USA. [4]Los Alamos National Laboratory, Los Alamos, NM, USA. [5]Department of Electrical and Computer Engineering, University of California San Diego, La Jolla, CA, USA. [6]Department of Physics, Tsinghua University, Beijing, People's Republic of China. [7]College of Physics and Optoelectronic Engineering, Shenzhen University, Shenzhen, People's Republic of China. [8]Department of Bioengineering, University of California San Diego, La Jolla, CA, USA. [9]These authors contributed equally: Yusheng Lei, Yimu Chen. ✉e-mail: shengxu@ucsd.edu

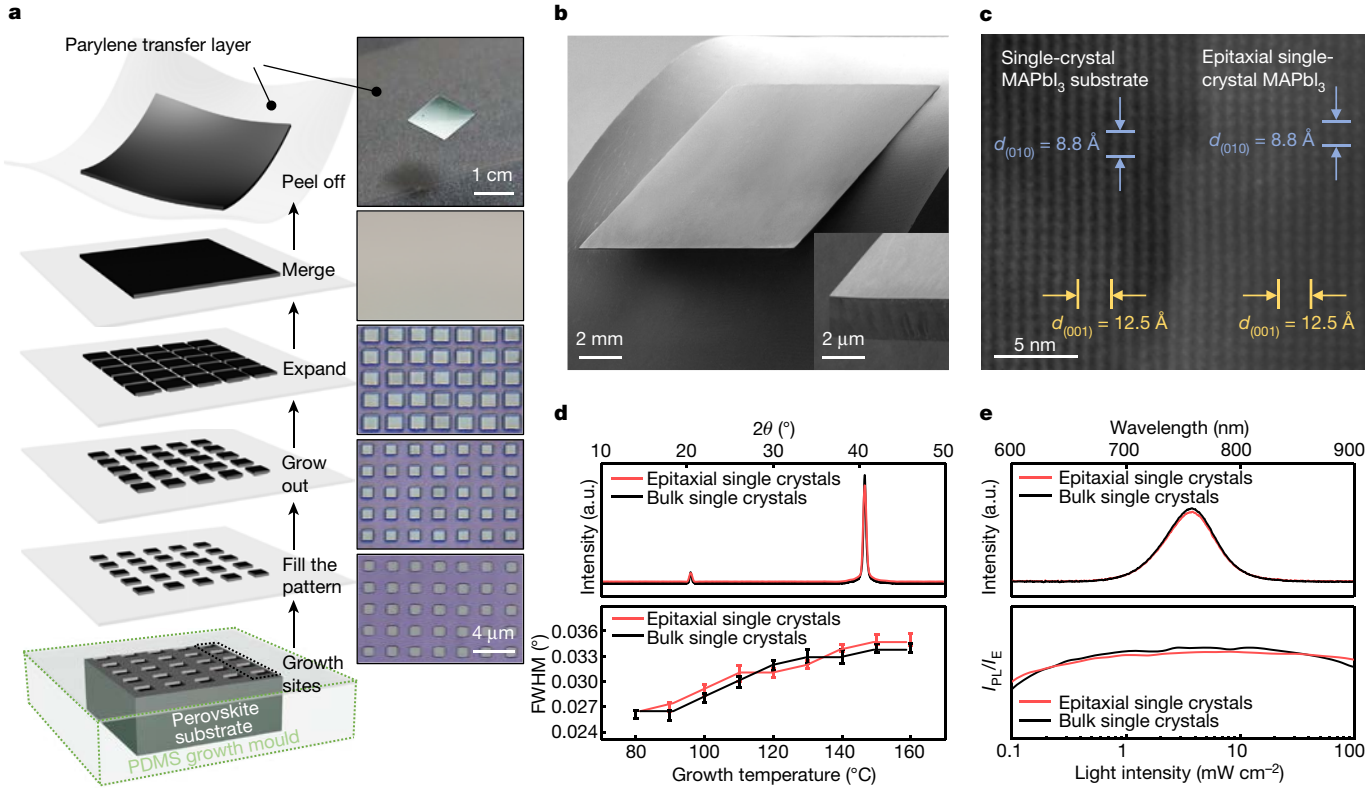

Fig. 1 | The lithography-assisted epitaxial-growth-and-transfer method for fabricating high-quality, single-crystal hybrid perovskite thin films. **a**, Schematics (left) and corresponding optical images (right) showing the solution-based epitaxial growth, merging and transferring processes of the single-crystal perovskite thin film. The bottom four optical images share the same scale bar, 4 μm. **b**, SEM images showing a single-crystal $MAPbI_3$ thin film with dimensions of about 1 cm × 1 cm × 2 μm on a bent PDMS substrate. Inset: magnified cross-section of the thin film without grain boundaries. **c**, A high-resolution TEM image showing the interfacial area of the homo-epitaxial single-crystal $MAPbI_3$. The epitaxial layer shows a well-aligned tetragonal lattice structure without dislocations. Contrast across the interface comes from different batches of growth solutions[33]. *d*, *d*-spacing. **d**, θ–2θ XRD comparison between the bulk single-crystal and the transferred epitaxial single-crystal thin film (on a PDMS substrate), showing that this growth-and-transfer method does not degrade the material crystallinity. The FWHM of the (400) peak in XRD ω-scan suggests high-quality, single-crystal perovskite thin films can be grown over a wide range of temperatures, which is applicable for different materials in the perovskite family. The error bars show the range from three measurements. **e**, PL and PL intensity comparisons between bulk single crystals and transferred epitaxial single-crystal thin films, showing the high quality of the transferred single-crystal thin films.

close tendency to that ratio of the bulk single crystal (Fig. 1e, bottom), providing additional evidence that this growth-and-transfer method will not cause noticeable non-radiative recombination or quenching in the transferred epitaxial single-crystal thin film[15,16].

The carrier diffusion length of the single-crystal thin film with different thicknesses has been calculated by measuring the carrier mobility and carrier lifetime using time-of-flight (ToF) and time-resolved PL (Extended Data Fig. 4 and Supplementary Discussion 5). The results show that the carrier mobility and the carrier lifetime increase with the crystal thickness. This can be attributed to the better crystal quality of the larger thickness, where there is a lower surface-to-volume ratio, a lower trap density, and smaller XRD and PL FWHM values in thicker films, as evidenced by thickness-dependent crystal-quality studies (Supplementary Fig. 13)[6]. The carrier diffusion length is estimated to saturate at about 5–7 μm, indicating that most charge carriers in thicker films are more likely to recombine rather than being collected[17].

Thickness-dependent external quantum efficiency (EQE) spectra have been measured and are shown in Fig. 2a, with the integrated current densities plotted in the inset. For a film thickness in the range of about 600 nm to about 2 μm, increasing the thickness improves the EQE, which should be due to the enhanced light harvesting and the better crystal quality of thick materials. In the roughly 2 μm to 5 μm range, even though the crystal quality is still improved, the carrier collection efficiency becomes the dominant limiting factor, and the EQE decreases as the thickness increases. Current density–voltage (*J*–*V*) measurements under 1-sun illumination of single-crystal $MAPbI_3$-based photovoltaic devices in Fig. 2b show a similar trend. When the single-crystal absorber thickness is below 2 μm, increasing the single-crystal absorber thickness can enhance the light absorption and therefore the current density. When the single-crystal absorber thickness is above 2 μm, the light absorption saturates (Supplementary Fig. 14). Further increasing the single-crystal absorber thickness will reduce only the fill factor (FF) and the open-circuit voltage (V_{OC}) (inset of Fig. 2b), which is due to the strong interfacial charge accumulation caused by the weaker build-in field in the thicker films. Note that in Fig. 2b, the source of the V_{OC} data for the *J*–*V* curves is different from that of the V_{OC} data in the inset. The inset data are from in situ-fabricated devices with untransferred single-crystal films, where any possible confounding factors from transfer steps besides the thickness can be minimized (Supplementary Discussion 6 and Supplementary Fig. 15).

We plot the slope of the *J*–*V* curve near the high-internal-field region (that is, the short-circuit current condition) and the low-internal-field region (that is, the V_{OC} condition) as a function of the absorber thickness (Fig. 2c). Owing to the small contributions from extrinsic resistance (Supplementary Fig. 16), the slopes near these two regions can serve as an indication of charge collection efficiency[18]. Ideally, a steep slope near the low-internal-field region and a close-to-zero slope near the high-internal-field region represent fast carrier transport and efficient charge collection. We find that devices with

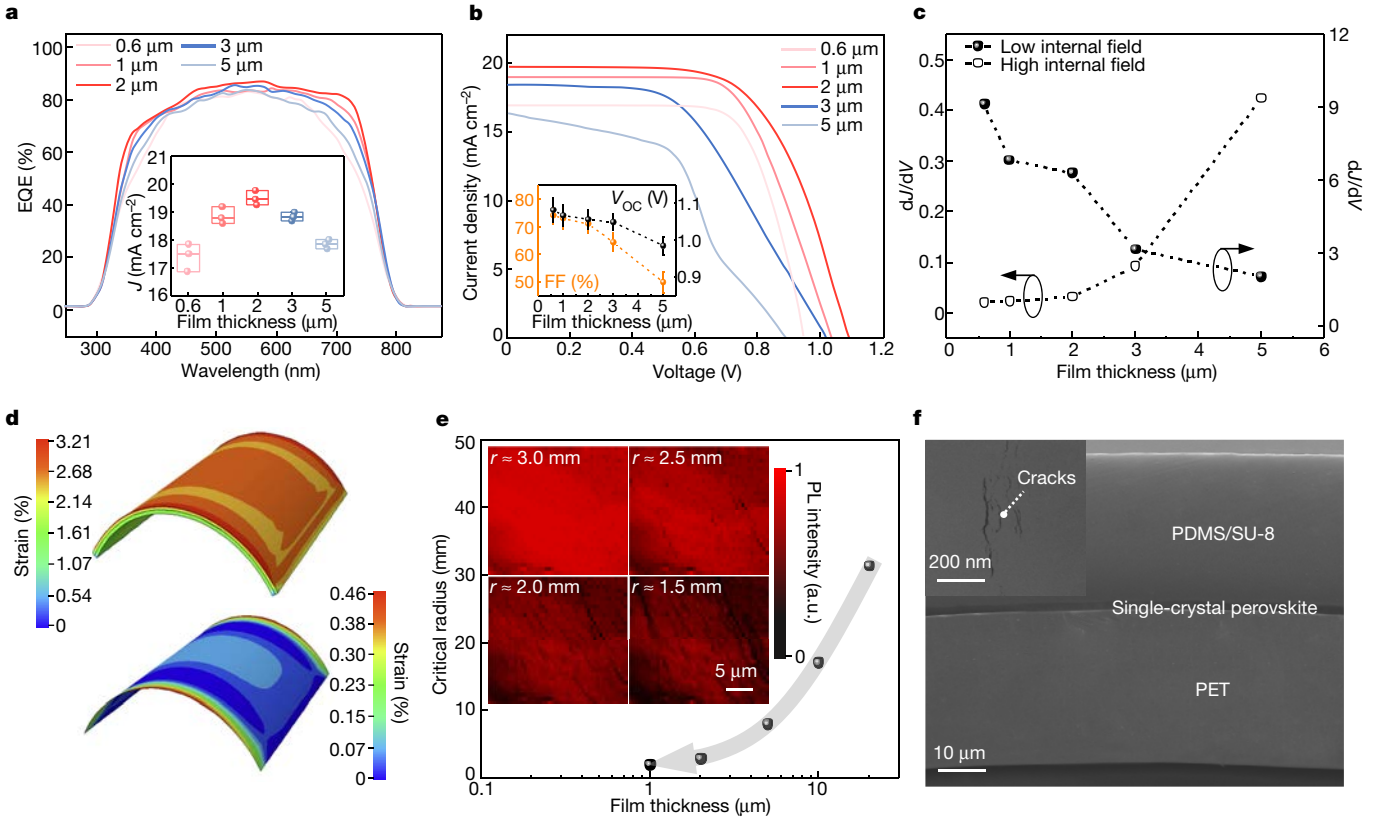

Fig. 2 | Thickness-dependent carrier transport and mechanical properties of the single-crystal hybrid perovskite. a, EQE measurements of the single-crystal hybrid perovskite with different thicknesses. Efficiency loss is observed when the film is either too thin or too thick, due to insufficient absorption or carrier collection, respectively. Inset: the integrated current density from the EQE measurements. Each box contains three data points with a maximum value (top line), a mean value (middle line) and a minimum value (bottom line). The efficiency loss leads to a low short-circuit current density (J_{SC}). **b**, *J*–*V* measurements of single-crystal $MAPbI_3$ photovoltaics with different absorber thicknesses fabricated using this growth-and-transfer method. The inset shows a decrease in both FF and V_{OC} with increasing absorber thickness; specifically, the inset V_{OC} results come from in situ devices. The error bars show the range from three measurements. **c**, *J*–*V* slopes at the low and high internal fields with different absorber thicknesses. Increasing the absorber thickness will cause a field-dependent charge collection at both the V_{OC} and J_{SC} regions. **d**, Finite element analysis of the single-crystal perovskite thin film with an NMP design at a bending radius of 2.5 mm. The top image shows the strain distribution in the entire sandwich structure, where the bending strain mostly occurs in the PET and SU-8/PDMS layers. The bottom image shows the strain distribution in the sandwiched single-crystal perovskite layer with all other layers hidden, where the maximum strain in the single-crystal perovskite layer is around 0.36%. **e**, Flexibility test results of the NMP design with different single-crystal perovskite film thicknesses. A smaller thickness leads to a smaller bending radius, which shows the remarkable flexibility of these brittle crystals. Inset: PL images show morphologies and cracks of the film at different bending radii. **f**, SEM images at a bending radius of about 2.5 mm, showing the relative thickness of different layers in the NMP design. The inset shows a magnified cross-section of the single-crystal $MAPbI_3$, illustrating the onset of fracture.

a thickness of 600 nm to 2 μm present efficient charge extraction: further increasing the film thickness will reduce the net field across the film. Therefore, the collection has to rely more on the carrier self-diffusion rather than field-driven drifting, where any potential barriers from trap states will substantially decrease the collection efficiency. Consideration of all the factors discussed leads to the conclusion that the optimal thickness for the single-crystal $MAPbI_3$ thin film used in this study is about 2 μm (see Supplementary Table 1 for more details).

Controlling the thickness of a single-crystal hybrid perovskite thin film can also tailor its mechanical properties. For a general material:

$$\sigma_{st} \propto \frac{Eh}{2r}$$

where σ_{st} is the maximum stress of the material, E is the Young's modulus, h is the thickness and r is the bending radius. Reducing the material thickness offers clear benefits in flexibility. Further enhancement of the device integrity can be achieved by placing the film on the neutral mechanical plane (NMP) (Supplementary Discussion 7), and the minimal bending radius for a roughly 2-μm-thick single-crystal film can reach about 2.5 mm (Extended Data Fig. 5).

Figure 2d shows the simulated strain distribution (maximum principal logarithmic strain) in a polyethylene terephthalate (PET)–$MAPbI_3$–SU-8/polydimethylsiloxane (PDMS) sandwich (top) as well as only the perovskite layer extracted from the NMP (bottom) when they are bent at a radius of 2.5 mm (see Supplementary Fig. 17 for other bending radii). The maximum principal strain in the majority of the single-crystal $MAPbI_3$ is less than 0.25%; the largest value occurs near the edge due to Poisson effects with a value of about 0.36%, which is close to the fracture strain of this material[19]. Mechanical tests clearly show the outstanding flexibility of single-crystal $MAPbI_3$ thin films under the NMP design (Fig. 2e; see Supplementary Fig. 18 for details). PL mapping of a roughly 2-μm-thick single-crystal $MAPbI_3$ with the NMP design under different bending radii shows that cracks begin to appear when the bending radius reaches about 2.5 mm (Fig. 2e, inset). Corresponding cross-sectional SEM images also show the onset of fractures at a bending radius of about 2.5 mm (Fig. 2f). The onset of the fractures is further confirmed by the *I*–*V* measurements under different bending radii (Supplementary Fig. 19), demonstrating the excellent flexibility and agreement with the simulations.

By feeding a continuous flow of precursors of different compositions (Extended Data Fig. 6; see Methods and Supplementary Discussion 1

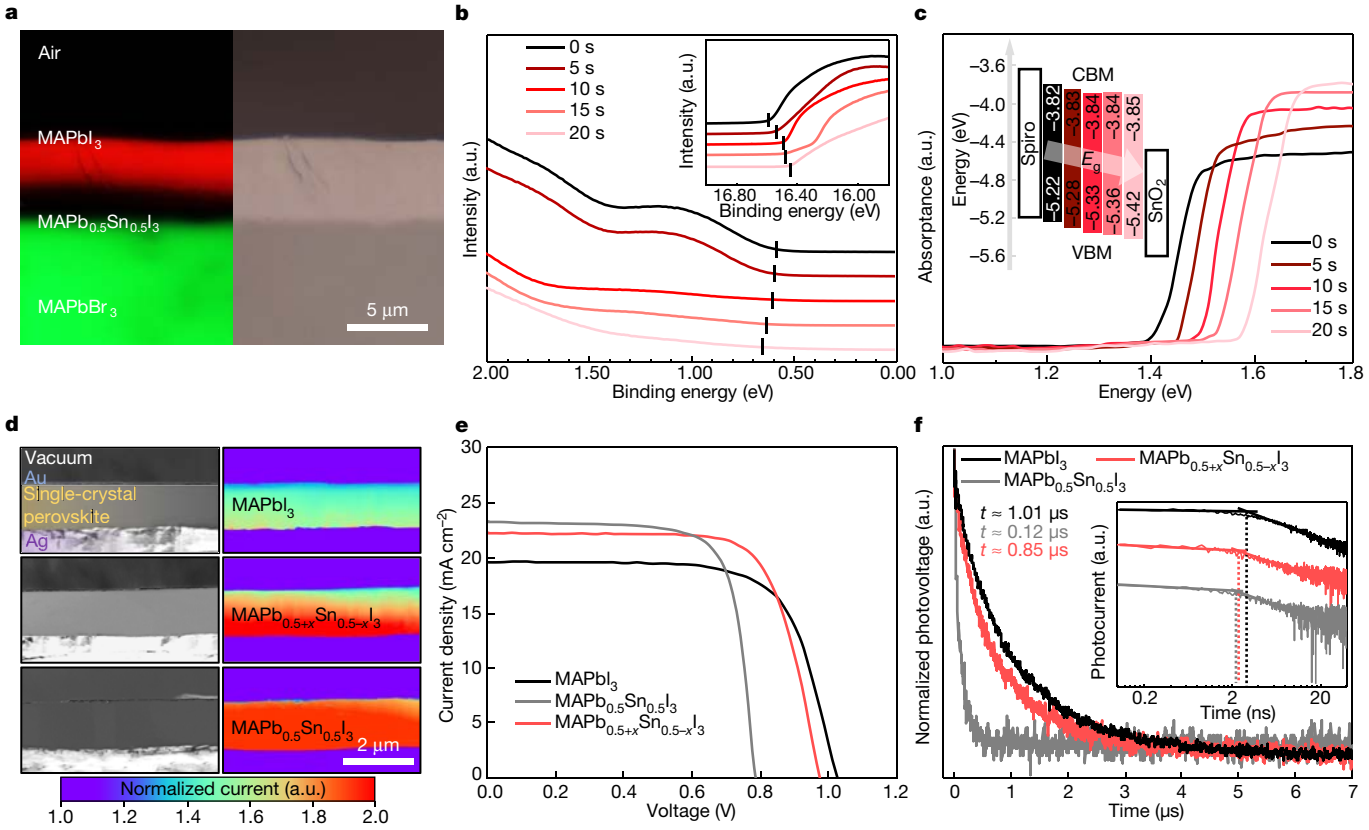

Fig. 3 | Bandgap-graded single-crystal perovskite thin films. a, A PL image (left) of the graded single-crystal $MAPb_{0.5+x}Sn_{0.5-x}I_3$ grown on a $MAPbBr_3$ substrate. $MAPbBr_3$ is chosen here as a representative example to show the compatibility of this growth-and-transfer method in the perovskite family. The dark tin-rich area is because of the infrared emission of the tin-alloyed $MAPbI_3$ being invisible on the camera. The contrast has been enhanced to better show the colour difference. A corresponding optical image (right) shows the graded $MAPb_{0.5+x}Sn_{0.5-x}I_3$ without noticeable structural interfaces. **b**, UPS measurements of samples at different growth times during the alloyed growth process: the bottom being $MAPb_{0.5}Sn_{0.5}I_3$ and the top being $MAPbI_3$. Inset: the VBM position is calculated from the low-binding-energy cut-off and the high-binding-energy cut-off, marked by the black vertical lines. **c**, UV–vis spectroscopy absorption of single-crystal thin films with the same composition as the surface composition of the graded structure at different growth times. Replacing tin with lead in the perovskite increases the bandgap. Inset: schematic showing the energy diagram based on calculations using the UPS and UV–vis data. E_g, bandgap energy; Spiro, the hole transport layer 2,2′,7,7′-tetrakis-9,9′-spirobifluorene (spiro-MeOTAD). **d**, SEM images and corresponding EBIC mapping of cross-sections of three different single-crystal perovskites: $MAPbI_3$ (top), graded $MAPb_{0.5+x}Sn_{0.5-x}I_3$ (middle) and $MAPb_{0.5}Sn_{0.5}I_3$ (bottom). The EBIC results show uniform current intensities for $MAPbI_3$ and $MAPb_{0.5}Sn_{0.5}I_3$ and a gradient current intensity for graded $MAPb_{0.5+x}Sn_{0.5-x}I_3$. **e**, Representative J–V curves of $MAPbI_3$, $MAPb_{0.5}Sn_{0.5}I_3$ and graded $MAPb_{0.5+x}Sn_{0.5-x}I_3$ single-crystal photovoltaic devices. The $MAPb_{0.5+x}Sn_{0.5-x}I_3$ single-crystal photovoltaic device shows the best performance among the three, due to the enhanced J_{SC} and relatively high V_{OC}. **f**, Transient photovoltage measurements show that the graded single-crystal $MAPb_{0.5+x}Sn_{0.5-x}I_3$ shows a relatively long carrier lifetime due to the easier exciton separation and charged carrier collection facilitated by the graded bandgap. Inset: ToF measurements show that the carrier mobility in graded single-crystal $MAPb_{0.5+x}Sn_{0.5-x}I_3$ is close to that in the compositionally uniform single-crystal $MAPb_{0.5}Sn_{0.5}I_3$. The inflection points of the photocurrent curves are marked by the dotted lines.

for more details), bandgap-graded single-crystal hybrid perovskite thin films can be achieved. $MAPb_{0.5}Sn_{0.5}I_3$ is chosen as the upper limit of the tin alloying concentration in this study. The resulting graded bandgap, gradually transitioning from $MAPb_{0.5}Sn_{0.5}I_3$ to $MAPbI_3$, is evidenced by the clear red–infrared interface in the PL image (Fig. 3a, left, and Supplementary Fig. 20). The bandgap-graded single crystal is stable without noticeable lead ion or tin ion migration or change in concentration gradient driven under an electrical field (Supplementary Fig. 21). Note that unlike conventional heterojunctions, no structural interface exists in the graded layer (Fig. 3a, right). The trap density in the graded single crystal is comparable to that of a pure $MAPbI_3$ single crystal (Supplementary Fig. 13c) and almost two orders of magnitude lower than that of a heterojunction with an abrupt interface (Supplementary Fig. 22).

We combine ultraviolet photoelectron spectroscopy (UPS) and ultraviolet–visible spectroscopy (UV–vis) to characterize the energy band structure of the graded single crystal in the growth process (Supplementary Discussion 8 and Supplementary Fig. 23). The UPS data show that the valence band maximum (VBM) position becomes lower (Fig. 3b) and the UV–vis results reveal that the bandgap becomes larger (Fig. 3c) as the growth continues. The summarized band structure of the $MAPb_{0.5+x}Sn_{0.5-x}I_3$ graded single-crystal is presented by the inset schematics in Fig. 3c. As the growth progresses and more lead is incorporated into the crystal, the position of the VBM becomes lower, and the position of the conduction band minimum (CBM) also becomes lower, but not as dramatically as the VBM. The changes in VBM and CBM result in a gradually increasing bandgap from the bottom ($MAPb_{0.5}Sn_{0.5}I_3$) to the surface ($MAPbI_3$), and the band structure of $MAPb_{0.5+x}Sn_{0.5-x}I_3$ is also supported by first-principles calculations (Extended Data Fig. 7 and Supplementary Discussion 9).

Figure 3d shows electron-beam-induced current (EBIC) mapping results along the cross-sections of three different single crystals. The compositionally uniform $MAPb_{0.5}Sn_{0.5}I_3$ (Fig. 3d, bottom) generates a higher current than the compositionally uniform $MAPbI_3$ (Fig. 3d, top), indicating easier exciton formation, charge dissociation and charge collection in $MAPb_{0.5}Sn_{0.5}I_3$ owing to its lower bandgap and weaker exciton binding[20]. The graded $MAPb_{0.5+x}Sn_{0.5-x}I_3$ (Fig. 3d, middle) shows a gradually decreasing

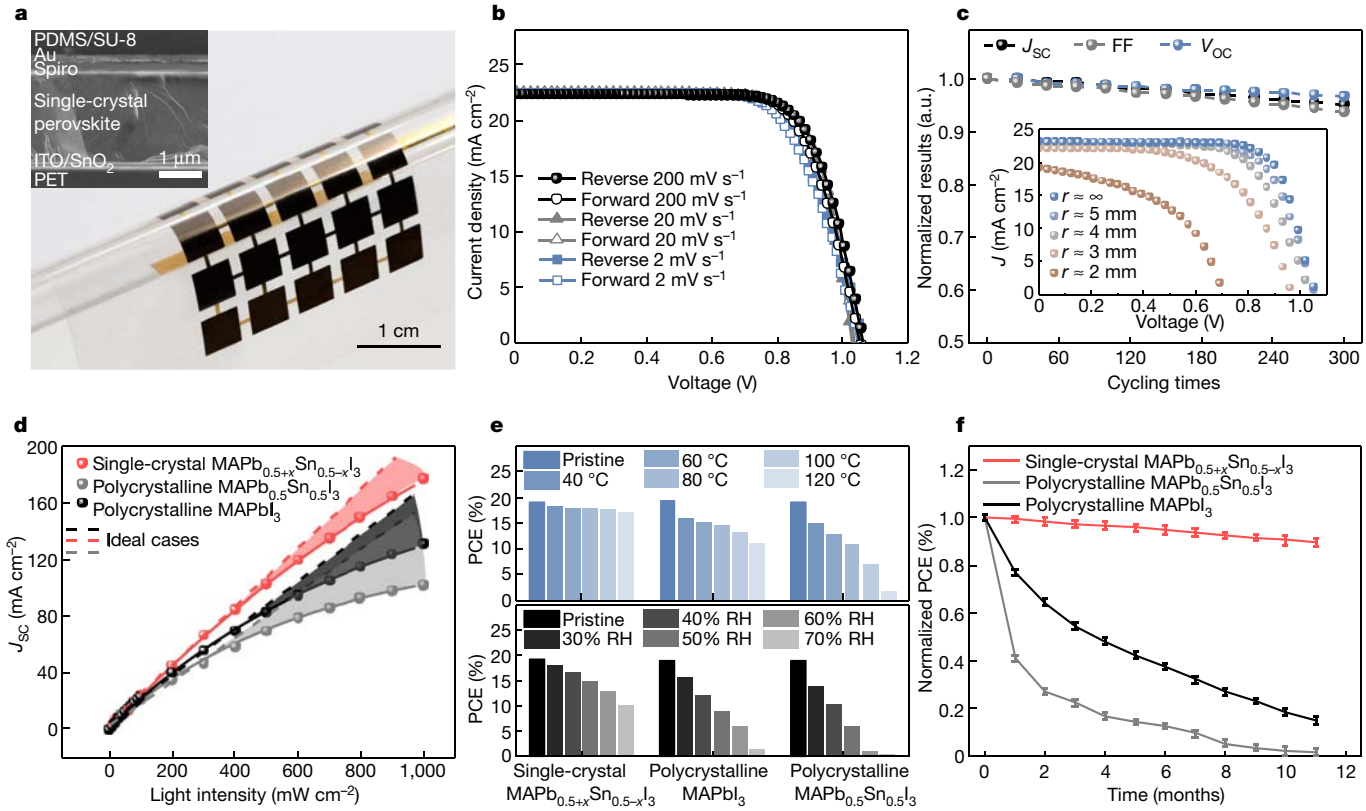

Fig. 4 | Flexible bandgap-graded single-crystal perovskite photovoltaics. **a**, An optical image showing an array of flexible single-crystal photovoltaic islands with a total working area of 6.25 cm^2 (0.5 cm × 0.5 cm × 25). Inset: a cross-sectional SEM image of the single-crystal perovskite photovoltaic device. **b**, Negligible *J*–*V* hysteresis in the graded single-crystal $MAPb_{0.5+x}Sn_{0.5-x}I_3$ photovoltaic devices. **c**, Cycling test results of the graded photovoltaic device at $r \approx 5$ mm. Inset: *J*–*V* curves at different bending radii. **d**, J_{SC} as a function of illumination intensity for graded single-crystal $MAPb_{0.5+x}Sn_{0.5-x}I_3$, polycrystalline $MAPb_{0.5}Sn_{0.5}I_3$, and polycrystalline $MAPbI_3$ photovoltaic devices. The polycrystalline devices tend to deviate from a linear relationship at higher intensities due to degradation in the absorber. The degree of dispersion is reflected by the shaded regions. **e**, Thermal and humidity stability test results of the graded single-crystal $MAPb_{0.5+x}Sn_{0.5-x}I_3$, polycrystalline $MAPb_{0.5}Sn_{0.5}I_3$ and polycrystalline $MAPbI_3$. Unencapsulated devices are used in only the humidity stability test. The ageing times for the thermal and humidity stability tests are 2 h and 30 min, respectively. RH, relative humidity. **f**, Long-term shelf-stability test results (over 11 months) of the graded single-crystal $MAPb_{0.5+x}Sn_{0.5-x}I_3$, polycrystalline $MAPb_{0.5}Sn_{0.5}I_3$ and polycrystalline $MAPbI_3$ photovoltaic devices in a dark dry box. A top SU-8/PDMS layer also covered the polycrystalline photovoltaic devices to maintain the same encapsulation. The single-crystal photovoltaic devices show much better stability in terms of PCE than their polycrystalline counterparts. Error bars show the range from three measurements with different aperture positions.

current when the tin content is reduced from 50% at the bottom to 0% at the surface. Any possible contribution from the top gold electrode that may have introduced a higher recombination rate has been excluded (Supplementary Fig. 24). EQE measurements show the median average current density in the graded absorber compared with $MAPbI_3$ and $MAPb_{0.5}Sn_{0.5}I_3$, indicating the existence of an engineered bandgap (Supplementary Fig. 25). *J*–*V* measurements reveal the overall performance of these three different absorbers (Fig. 3e). Both the $MAPb_{0.5}Sn_{0.5}I_3$ and the graded $MAPb_{0.5+x}Sn_{0.5-x}I_3$ absorbers give a higher short-circuit current density (J_{SC}) than $MAPbI_3$, as alloying tin with the lead decreases the bandgap and the exciton binding energy. However, $MAPb_{0.5}Sn_{0.5}I_3$ shows a much lower V_{OC} compared with $MAPbI_3$, because of its higher defect concentrations, shorter carrier lifetimes and lower bandgap. Surprisingly, the graded $MAPb_{0.5+x}Sn_{0.5-x}I_3$ gives a relatively high V_{OC} and has the best overall performance among the three absorbers (Supplementary Fig. 26).

We combine calculations and experiments to understand the high V_{OC} of the graded $MAPb_{0.5+x}Sn_{0.5-x}I_3$. The calculation results show a decrease in carrier effective mass (for both electrons and holes) when more tin is incorporated into lead perovskites (Extended Data Fig. 7). ToF results show that the carrier mobility in the graded $MAPb_{0.5+x}Sn_{0.5-x}I_3$ is on par with that in $MAPb_{0.5}Sn_{0.5}I_3$ (Fig. 3f, inset). However, transient photovoltage measurements show that the carrier lifetime in the graded structure is much higher than that in $MAPb_{0.5}Sn_{0.5}I_3$ (Fig. 3f), contradictory to our understanding that adding tin into lead perovskites normally results in a lower carrier lifetime because of the high recombination rate in tin perovskites[21,22]. We ascribe the measured high carrier lifetime in the $MAPb_{0.5+x}Sn_{0.5-x}I_3$ to its graded bandgap, which is similar to the built-in field of a p–n junction. The graded bandgap of the $MAPb_{0.5+x}Sn_{0.5-x}I_3$ facilitates the carrier separation, transport and collection with an extended carrier lifetime (Supplementary Discussion 10 and Supplementary Fig. 27)[23,24], resulting in a relatively high V_{OC}.

We integrate the single-crystal thin films in various devices. Single-crystal perovskite light-emitting diodes have been demonstrated using this growth-and-transfer method (Extended Data Fig. 8). The pixel size can range from 1 μm to 100 μm, with potential applications for flexible displays with tunable colour, high resolution, high stability and high quantum efficiency. Furthermore, this growth-and-transfer method allows the engineering of the material morphology and orientation[13]. A textured anti-reflective single-crystal perovskite photodetector shows improved performances over one with a flat surface (Extended Data Fig. 8). The focus of this study is photovoltaic devices. Shown in Fig. 4a is a flexible array of photovoltaic devices in an island-bridge layout[25], with each island a single-crystal perovskite photovoltaic device interconnected by the metallic bridges. The corresponding cross-sectional structure of an island is illustrated in the inset of Fig. 4a. The mode value of power conversion efficiency (PCE) of a 0.5 cm × 0.5 cm island under a 3 mm × 3 mm mask is 15–17% for single-crystal $MAPbI_3$, and 17–19% for graded single-crystal $MAPb_{0.5+x}Sn_{0.5-x}I_3$ (Supplementary Fig. 26).

The highest PCE that has been measured is 20.04% under the initial reverse scanning. To further improve the single-crystal device performance, surface/interface passivation and strategic layer design are needed. Most devices show negligible J–V hysteresis at different scan rates and directions (Fig. 4b). The entire array of graded single-crystal $MAPb_{0.5+x}Sn_{0.5-x}I_3$ photovoltaics shows an overall PCE of about 10.3% with a working area of about 9 cm^2 (Supplementary Fig. 28).

In mechanical testing, the flexible photovoltaic device undergoes bending–straightening cycles. The islands in the middle of the array experience the most bending (Supplementary Fig. 29) and are therefore selected to demonstrate the mechanical stability of the entire array (Fig. 4c; see Supplementary Fig. 30 for the other islands). At $r \approx 5$ mm, a small decrease in V_{OC} (from 100% to 96.5%) and J_{SC} (from 100% to 94.9%), and a decay in FF (from 100% to 93.7%) are observed after a 300-time cycle. The decrease may be due to the increase in series resistance caused by the interfacial delamination. Further decreasing r causes a substantial drop in V_{OC}, J_{SC} and FF, which possibly results from the material failure (for example, cracks in the absorber) (Fig. 4c, inset). Polycrystalline photovoltaics of the same device configuration show substantial performance degradation under the same cyclic bending tests (Supplementary Fig. 31), which may be caused by the fast material and device degradation at the grain boundaries during bending (Supplementary Discussion 11 and Supplementary Fig. 32)[26,27].

Stress-stability test results, in which the J_{SC} is measured as a function of light intensity, are presented in Fig. 4d. Owing to the lack of a way to realize lead–tin composition gradients in the polycrystalline structure without junction formation, only $MAPb_{0.5}Sn_{0.5}I_3$ and $MAPbI_3$ have been fabricated in polycrystalline photovoltaics for comparison (Supplementary Discussion 12). The relationship between J_{SC} and light intensity for the graded single-crystal $MAPb_{0.5+x}Sn_{0.5-x}I_3$ photovoltaics is close to linear, indicating good charge collection[28]. Single-crystal photovoltaics of graded $MAPb_{0.5+x}Sn_{0.5-x}I_3$, $MAPb_{0.5}Sn_{0.5}I_3$ and $MAPbI_3$ show similar stress stability (Supplementary Fig. 33). However, the J_{SC}–light intensity curves for polycrystalline $MAPb_{0.5}Sn_{0.5}I_3$ and $MAPbI_3$ photovoltaics tend to deviate from the linear relationship at higher light intensities, probably due to degradation facilitated by the presence of grain boundaries.

Figure 4e shows single-crystal photovoltaic devices have better stability than polycrystalline devices under different thermal and humidity conditions (see Supplementary Discussion 12 for the humidity control, and Supplementary Fig. 34 for additional humidity and thermal stability comparisons). Thermogravimetric analysis confirms that the single-crystal film decomposes at a higher temperature than the polycrystalline film (Supplementary Fig. 35). In situ X-ray photoelectron spectroscopy (XPS) results reveal that degradation factors (for example, pinholes and grain boundaries) in the polycrystalline structure facilitate oxygen and moisture diffusion, leading to a rapid oxidization of Sn^{2+} and overall degradation rate[22,29,30] (Extended Data Fig. 9). Besides, single-crystal devices show a slower decay than polycrystalline devices with the same measurement conditions and encapsulation in 1,000-h continuous illumination stability tests under 1-sun intensity by tracking the maximum power point[31,32] (Extended Data Fig. 10). Such a difference is attributed to the suppressed ion migration and the intrinsic slow self-doping effect in the single crystals (Supplementary Discussions 13 and 14). In addition, to manifest the difference in the single-crystal and polycrystalline perovskites, we replace the thermal/light sensitive 2,2′,7,7′-tetrakis-9,9′-spirobifluorene (spiro-MeOTAD) with the more stable poly(bis(4-phenyl)(2,4,6-trimethylphenyl)amine)[32]. The stability differences among those devices become even more pronounced (Supplementary Fig. 36). Finally, long-term shelf-stability studies (Fig. 4f and Supplementary Fig. 37) further prove that single-crystal devices have much better stability than their polycrystalline counterparts regardless of the composition (Supplementary Discussion 14 and Supplementary Figs. 38–41).

Online content

Any methods, additional references, Nature Research reporting summaries, source data, extended data, supplementary information, acknowledgements, peer review information; details of author contributions and competing interests; and statements of data and code availability are available at https://doi.org/10.1038/s41586-020-2526-z.

1. Yang, W. S. et al. Iodide management in formamidinium-lead-halide-based perovskite layers for efficient solar cells. *Science* **356**, 1376–1379 (2017).
2. Lin, K. et al. Perovskite light-emitting diodes with external quantum efficiency exceeding 20 per cent. *Nature* **562**, 245–248 (2018).
3. Feng, J. et al. Single-crystalline layered metal-halide perovskite nanowires for ultrasensitive photodetectors. *Nat. Electron.* **1**, 404–410 (2018).
4. National Renewable Energy Laboratory. *Best Research-Cell Efficiency Chart* https://www.nrel.gov/pv/cell-efficiency.html (NREL, US Department of Energy, 2020).
5. Wang, Q. et al. Large fill-factor bilayer iodine perovskite solar cells fabricated by a low-temperature solution-process. *Energy Environ. Sci.* **7**, 2359–2365 (2014).
6. Liu, Z. et al. Gas–solid reaction based over one-micrometer-thick stable perovskite films for efficient solar cells and modules. *Nat. Commun.* **9**, 3880 (2018).
7. Jiang, Q. et al. Surface passivation of perovskite film for efficient solar cells. *Nat. Photon.* **13**, 460–466 (2019); correction **13**, 500 (2019).
8. Leblebici, S. Y. et al. Facet-dependent photovoltaic efficiency variations in single grains of hybrid halide perovskite. *Nat. Energy* **1**, 16093 (2016).
9. Zhang, W. et al. Enhanced optoelectronic quality of perovskite thin films with hypophosphorous acid for planar heterojunction solar cells. *Nat. Commun.* **6**, 10030 (2015).
10. Zheng, G. et al. Manipulation of facet orientation in hybrid perovskite polycrystalline films by cation cascade. *Nat. Commun.* **9**, 2793 (2018).
11. Chen, Z. et al. Thin single-crystal perovskite solar cells to harvest below-bandgap light absorption. *Nat. Commun.* **8**, 1890 (2017).
12. Lee, L. et al. Wafer-scale single-crystal perovskite patterned thin films based on geometrically-confined lateral crystal growth. *Nat. Commun.* **8**, 15882 (2017).
13. Lei, Y. et al. Controlled homoepitaxial growth of hybrid perovskites. *Adv. Mater.* **30**, 1705992 (2018).
14. Chen, Y. et al. Strain engineering and epitaxial stabilization of halide perovskites. *Nature* **577**, 209–215 (2020).
15. Zou, W. et al. Minimising efficiency roll-off in high-brightness perovskite light-emitting diodes. *Nat. Commun.* **9**, 608 (2018).
16. Richter, J. M. et al. Enhancing photoluminescence yields in lead halide perovskites by photon recycling and light out-coupling. *Nat. Commun.* **7**, 13941 (2016).
17. Gong, X. et al. Contactless measurements of photocarrier transport properties in perovskite single crystals. *Nat. Commun.* **10**, 1591 (2019).
18. Tsai, H. et al. Design principles for electronic charge transport in solution-processed vertically stacked 2D perovskite quantum wells. *Nat. Commun.* **9**, 2130 (2018).
19. Ćirić, L. et al. Mechanical response of $CH_3NH_3PbI_3$ nanowires. *Appl. Phys. Lett.* **112**, 111901 (2018).
20. Bokdam, M. et al. Role of polar phonons in the photo excited state of metal halide perovskites. *Sci. Rep.* **6**, 28618 (2016).
21. Noel, N. K. et al. Lead-free organic-inorganic tin halide perovskites for photovoltaic applications. *Energy Environ. Sci.* **7**, 3061–3068 (2014).
22. Tong, J. et al. Carrier lifetimes of >1 μs in Sn-Pb perovskites enable efficient all-perovskite tandem solar cells. *Science* **364**, 475–479 (2019).
23. Dullweber, T., Rau, U. & Schock, H. A new approach to high-efficiency solar cells by band gap grading in Cu(In, Ga)Se_2 chalcopyrite semiconductors. *Sol. Energy Mater. Sol. Cells* **67**, 145–150 (2001).
24. Hutchby, J. A. & Fudurich, R. L. Theoretical analysis of $Al_xGa_{1-x}As$-GaAs graded band-gap solar cell. *J. Appl. Phys.* **47**, 3140–3151 (1976).
25. Wang, C., Wang, C., Huang, Z. & Xu, S. Materials and structures toward soft electronics. *Adv. Mater.* **30**, 1801368 (2018).
26. Wang, S., Jiang, Y., Juarez-Perez, E. J., Ono, L. K. & Qi, Y. Accelerated degradation of methylammonium lead iodide perovskites induced by exposure to iodine vapour. *Nat. Energy* **2**, 16195 (2017).
27. Yun, J. S. et al. Humidity-induced degradation via grain boundaries of $HC(NH_2)_2PbI_3$ planar perovskite solar cells. *Adv. Funct. Mater.* **28**, 1705363 (2018).
28. Tsai, H. et al. Light-induced lattice expansion leads to high-efficiency perovskite solar cells. *Science* **360**, 67–70 (2018).
29. Ke, W. & Kanatzidis, M. G. Prospects for low-toxicity lead-free perovskite solar cells. *Nat. Commun.* **10**, 965 (2019).
30. Chen, M. et al. Highly stable and efficient all-inorganic lead-free perovskite solar cells with native-oxide passivation. *Nat. Commun.* **10**, 16 (2019).
31. Domanski, K., Alharbi, E. A., Hagfeldt, A., Grätzel, M. & Tress, W. Systematic investigation of the impact of operation conditions on the degradation behaviour of perovskite solar cells. *Nat. Energy* **3**, 61–67 (2018).
32. Ono, L. K., Qi, Y. & Liu, S. F. Progress toward stable lead halide perovskite solar cells. *Joule* **2**, 1961–1990 (2018).
33. Liu, M., Jing, D., Zhou, Z. & Guo, L. Twin-induced one-dimensional homojunctions yield high quantum efficiency for solar hydrogen generation. *Nat. Commun.* **4**, 2278 (2013).

Methods

Materials

The materials used in this study were purchased for direct use without further purification, which include lead iodide (PbI_2, 99.99%, Tokyo Chemical Industry), methylammonium iodide (MAI, 99.9%, Greatcell Solar), tin iodide (SnI_2, anhydrous 99.99%, Sigma Aldrich), tin(II) chloride dihydrate ($SnCl_2{\cdot}2H_2O$, 98%, Sigma Aldrich), spiro-MeOTAD (LT-S922, Luminescence Technology), 4-tert-butylpyridine (Sigma Aldrich), bis(trifluoromethylsulfonyl)amine lithium salt (Sigma Aldrich), chlorobenzene (TCI America), anhydrous acetonitrile (99.8%, Sigma Aldrich), anhydrous ethanol (Sigma Aldrich), anhydrous dimethylformamide (DMF, 99.8%, Sigma Aldrich), anhydrous gamma-butyrolactone (Sigma Aldrich), indium tin oxide-coated polyethylene terephthalate (PET/ITO, Zhuhai Kaivo Optoelectronic Technology, Visiontek Systems), poly(pyromellitic dianhydride-co-4,4′-oxydianiline) (polyimide precursor, Sigma Aldrich), 1-methoxy-2-propanol acetate (SU-8, MicroChem) and polydimethylsiloxane (PDMS, monoglycidyl ether terminated, average molecular weight $M_n \approx 5{,}000$, Sigma Aldrich).

Device fabrication

Patterned ITO/PET substrates were first cleaned with water, acetone and isopropyl alcohol in an ultrasonication bath for 15 min, respectively. The substrates were then treated by oxygen plasma for 3 min before coating. The $SnCl_2$ solution (0.045 g $SnCl_2{\cdot}2H_2O$ in 2 ml of anhydrous ethanol) was spin-coated at 5,000 r.p.m. for 40 s followed by 2 h of 150 °C baking to serve as the electron transporting layer. The coated substrates were then used for single-crystal hybrid perovskite thin-film transfer in the lithography-assisted epitaxial-growth-and-transfer method (see Supplementary Discussion 1 for details). After all the transferring and etching steps, spiro-MeOTAD solution was spin-coated as the hole transporting layer at 3,500 r.p.m. for 30 s onto the ITO/SnO_2/single-crystal perovskite substrate. The obtained samples were loaded into a vacuum chamber for gold deposition. A mixture of SU-8 and PDMS was coated onto the gold layer for overnight curing. For the polycrystalline $MAPbI_3$ device fabrication, 0.2026 g of MAI and 0.5877 g of PbI_2 were dissolved into 1 ml of DMF/dimethyl sulfoxide (DMSO) solvent (DMF:DMSO = 19:1) to form a clear precursor solution. It has been found that the traditional 4:1 or 9:1 (refs. [34,35]) solvent ratio sometimes results in milky coloured films. Then 75 µl of the precursor was dropped on top of a prepared substrate (ITO/SnO_2) and the spin speed was set at 6,000 r.p.m. for 30 s. At the seventh second, 500 µl of diethyl ether was quickly dropped at the centre of the substrate. After spin coating, the substrate was transferred onto a hotplate (110 °C) for 5 min. A black $MAPbI_3$ polycrystal thin film was achieved. For $MAPb_xSn_{1-x}I_3$, MAI was fixed at 0.2026 g for all of the different compositions. The calculated amounts of SnI_2 and PbI_2 were dissolved into 1 ml of DMF/DMSO solvent (DMF:DMSO = 19:1) to form clear precursor solutions. Then 75 µl of precursor solution was dropped on top of a prepared substrate (ITO/SnO_2) and the spin speed was set at 6,000 r.p.m. for 30 s. At the tenth second, 500 µl of diethyl ether was quickly dropped at the centre of the substrate. After spin coating, the substrate was transferred on a hotplate (110 °C) for 5 min. A black $MAPb_xSn_{1-x}I_3$ polycrystal thin film was achieved. It is worth pointing out that if any cloudy or milky colour appears, the dropping of the antisolvent should be moved to a slightly earlier time.

Characterization

All SEM images were taken using a Zeiss Sigma 500 SEM. All optical images were taken using a Zeiss Axio Imager Optical Microscope. The XRD data were measured by a Rigaku 393 Smart lab diffractometer equipped with a Cu Kα1 radiation source ($\lambda = 0.15406$ nm) and a Ge 394 (220 × 2) monochromator. The TEM images were taken using an FEI 200 kV Sphera microscope. Samples for the TEM were prepared using a frozen focused ion beam (FEI Scios Dual Beam FIB/SEM). *J*–*V* measurements were carried out using a Keithley 2400 source meter under a simulated air mass of 1.5 irradiation (100 mW cm^{-2}) and a xenon-lamp-based solar simulator (Oriel LCS-100). The same shadow mask was used during the device measurement to avoid edge effects for small-area photovoltaic devices. A monocrystalline silicon photovoltaic device (Newport 532, ISO1599, calibrated by the National Institute of Standards and Technology) was used for light intensity calibration before all measurements. EQE data were collected by illuminating the device under monochromatic light using a tungsten source (chopped at 150 Hz) while collecting the photocurrent by a lock-in amplifier in the a.c. mode. The light source spectrum response was corrected by a calibrated silicon diode (FDS1010, Thorlab). Energy dispersive X-ray spectroscopy linear scanning was performed through a field emission environmental SEM (FEI/Phillips XL30 ESEM) system. The EBIC was collected using a FEI Scios Dual Beam microscope with a Mighty EBIC 2.0 controller (Ephemeron Labs) and a Femto DLPCA-200 preamplifier. For the cross-section configuration measurements, the thin single-crystal perovskite sample was pre-deposited with electrodes on two flat sides by electron-beam evaporation. Then, the sample was loaded onto the EBIC holder fixed by fast-dry silver epoxy. The acceleration voltage and current were 15 kV and 15 pA, respectively. The EBIC and SEM images of the same region of interest were collected simultaneously. UPS and XPS measurements were carried out on the surface of the epitaxial single-crystal perovskites films using Kratos AXIS Supra with a He I (21.22 eV) source under 10^{-8} torr chamber pressure. UV–vis and absorption spectra were collected using a Perkin Elmer Lambda 1050 UV–vis system under the reflection mode. Adhesion force tests and cycling bending tests were performed using an Instron Machine (5965 Dual Column Testing Systems) system. For cycling bending tests, a speed mode was used to fix the bending curvature of the device with an extrusion speed of 1 mm min^{-1}. Bending curvature mapping measurements were finished by an HDI Advance three-dimensional scanner (GOMEASURE3D). The devices were fixed onto a series of three-dimensional-printed plastic rods with designed radii to carry out the curvature mapping experiments. ToF was measured by the extraction time in the transient photocurrent to calculate the carrier mobility. An external bias of 0.5 V was used to power the devices with a resistor connected in series. Transient photovoltages were measured with an oscilloscope (Agilent MSO6104A Channel Mixed Signal). A pulsed laser with a pulse width of less than 10^{-10} s was used as the light source. PL and time-resolved PL measurements were performed with a confocal microscopy system focusing a monochromatic 6-ps-pulsed laser with a ×4 objective lens (numerical aperture 0.13) under 1-sun intensity. Samples were measured in a dark environment at room temperature. The trap density was measured using the space-charge limited current method by a Keithley 2400 source meter and a customized probe station in a dark environment. Devices were deposited with gold electrodes by electron-beam evaporation. Thermogravimetric analysis was conducted with a Netzsch STA 449 F1 Jupiter system. All samples were prepared on general glass slides without any other materials introduced. The temperature increase rate was kept at about 1 °C min^{-1} to avoid possible fluctuations.

Data availability

The data that support the findings of this study are available from the corresponding authors on reasonable request.

34. Ahn, N. et al. Highly reproducible perovskite solar cells with average efficiency of 18.3% and best efficiency of 19.7% fabricated via Lewis base adduct of lead (II) iodide. *J. Am. Chem. Soc.* **137**, 8696–8699 (2015).
35. Zhao, P. et al. Antisolvent with an ultrawide processing window for the one-step fabrication of efficient and large-area perovskite solar cells. *Adv. Mater.* **30**, 1802763 (2018).

Acknowledgements We thank S. Shrestha for discussions on the polycrystalline device fabrication, S. Wang for analysis and discussions on the UPS, Y. Wang for discussions on the

adhesion force measurement, J. Wu for analysis and discussion of the EBIC and S. Xiang for feedback on the manuscript preparation. This work was supported by the start-up fund by University of California San Diego. D.P.F. acknowledges California Energy Commission award no. EPC-16-050. The microfabrication involved in this work was in part performed at the San Diego Nanotechnology Infrastructure (SDNI) of UCSD, a member of the National Nanotechnology Coordinated Infrastructure, which was supported by the National Science Foundation (grant number ECCS-1542148). This characterization work was performed, in part, at the Center for Integrated Nanotechnologies, an Office of Science User Facility operated for the US Department of Energy (DOE) Office of Science by Los Alamos National Laboratory (contract 89233218CNA000001) and Sandia National Laboratories (contract DE-NA-0003525).

Author contributions S.X. and Y. Lei conceived the idea. Y. Lei and Y.C. contributed to the growth and transfer method. Y. Lei and Y.C. took the optical and SEM images. Y. Lei and R.Z. carried out the photovoltaic-related characterizations. Y. Lei carried out the EBIC measurements. R.Z. carried out the XRD characterizations. Yuheng Li and K.Y. carried out the DFT calculations. Q.Y. and J.L. contributed to the TEM and XPS characterizations. S.L. carried out the finite element analysis. Y. Lei, Y.Y., H.T., W.C., K.W., Y. Luo, D.P.F., S.A.D., J.Y., W.N. and Y.-H.L. contributed to the carrier dynamic measurement and analysis. Y. Lei, Y.C., Y.G. and Chunfeng Wang contributed to the device fabrication. Y. Lei, S.L., M.L. and M.P. contributed to the flexibility characterizations. X.Z. carried out the FDTD calculations. Y. Lei, Chonghe Wang, H.H., Yang Li, B.Q. and Z.Z. contributed to the schematics and photographs. All authors contributed to discussing the data and commenting on the manuscript.

Competing interests The authors declare no competing interests.

Additional information

Supplementary information is available for this paper at https://doi.org/10.1038/s41586-020-2526-z.

Correspondence and requests for materials should be addressed to S.X.

Peer review information *Nature* thanks Hyunhyub Ko and the other, anonymous, reviewer(s) for their contribution to the peer review of this work.

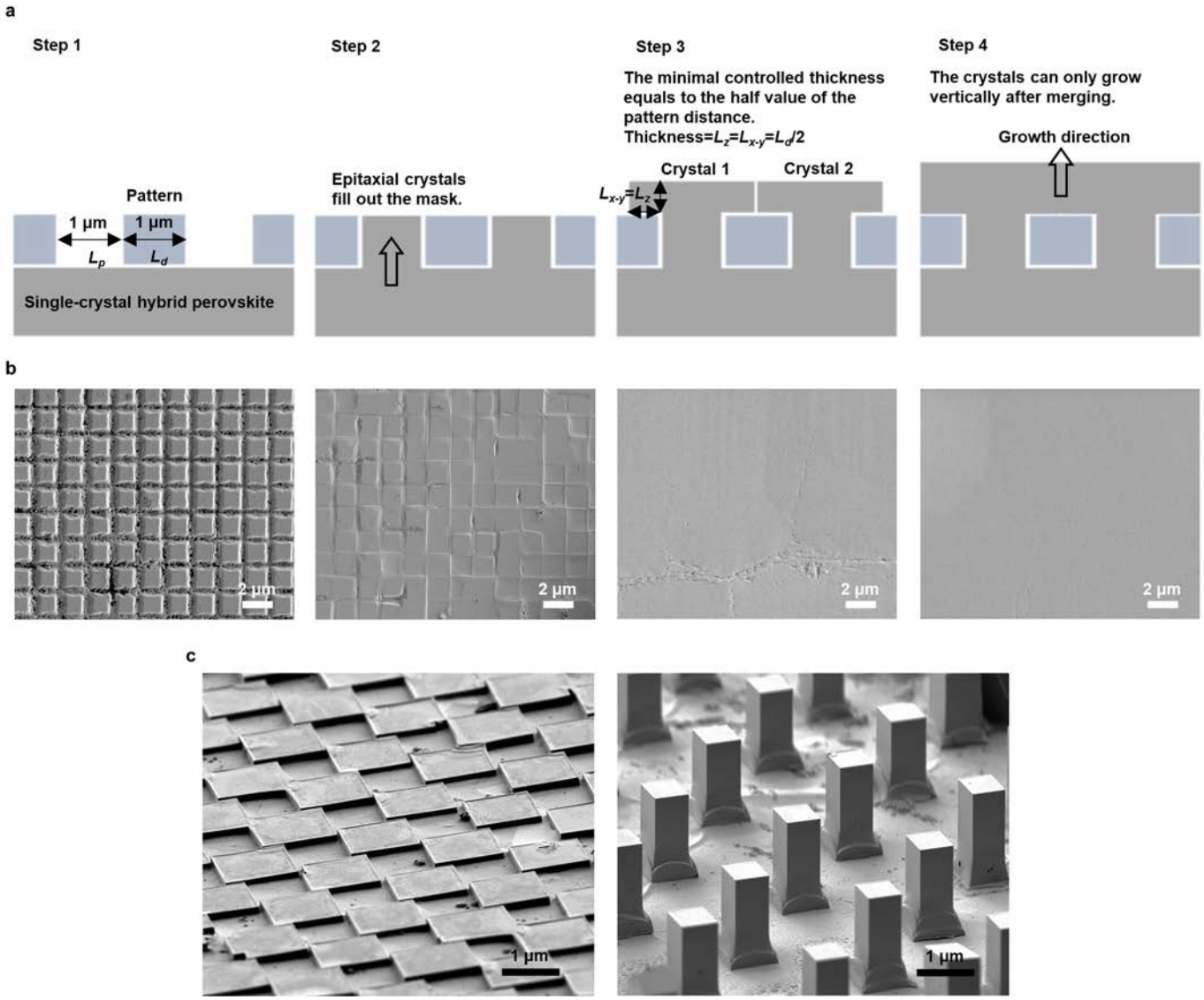

Extended Data Fig. 1 | The mechanism of the lithography-assisted epitaxial-growth-and-transfer method. a, Detailed schematic growth steps. L_p, pattern width; L_d, distance between two patterns; $L_{x\text{-}y}$, growth length in the x–y plane; L_z, growth length in the vertical z direction. **b**, Detailed epitaxial merging steps shown by SEM images (top view). First, individual single-crystals grow out of the mask. The lattice orientation of the epitaxial crystals is the same, which is controlled by the substrate. Then the individual crystals gradually expand and contact with each other. No lattice tilting or twisting can be found. Finally, completely merged single-crystal thin films are formed, where no grain boundaries can be seen. **c**, Titled SEM images of different growth behaviour under different growth temperatures and precursor concentrations. Low temperature and concentration can result in thin films (left), whereas high temperature and concentration lead to rods (right).

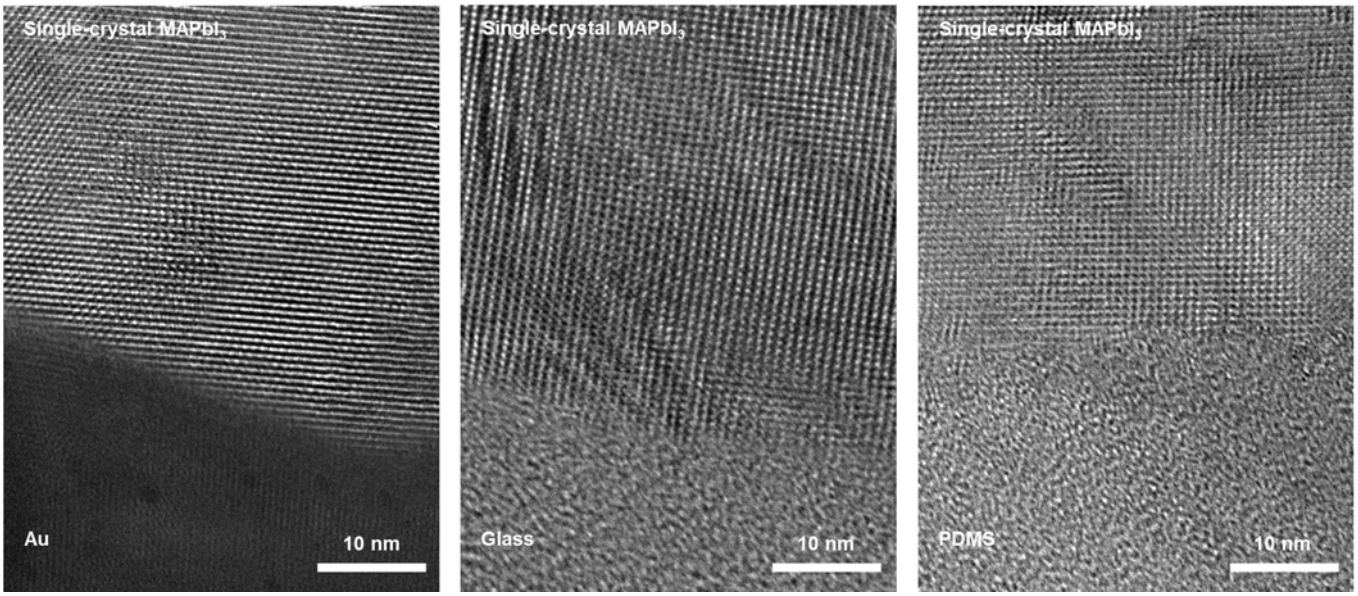

Extended Data Fig. 2 | Characterizations of interfacial crystal quality. High-resolution TEM studies of transferred single-crystal $MAPbI_3$ on different substrates (for example, gold for metals, glass for oxides and PDMS for polymers) using this growth-and-transfer method. The results show that there is no obvious lattice dislocation or polycrystalline structure formed at the interface, indicating that the re-adhesion/re-growth process maintains the single-crystal properties of the transferred materials.

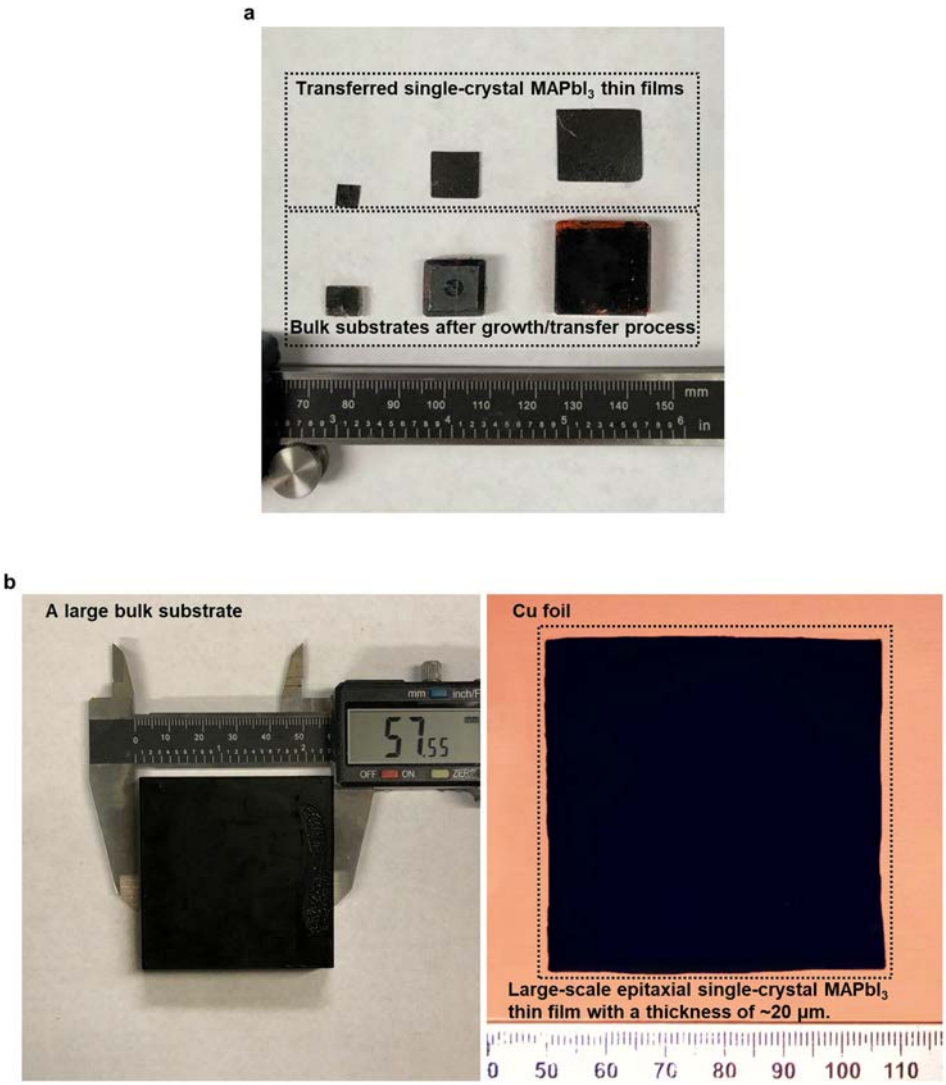

Extended Data Fig. 3 | Scaling up the fabrication method. a, Freestanding transferred single-crystal $MAPbI_3$ thin films fabricated by soft polymer masks and corresponding bulk substrates. **b**, A large bulk substrate (left) that is used to epitaxially grow the single-crystal $MAPbI_3$ thin film (left) and a transferred single-crystal $MAPbI_3$ thin film using a rigid copper foil (20 μm thick) as the mask (right).

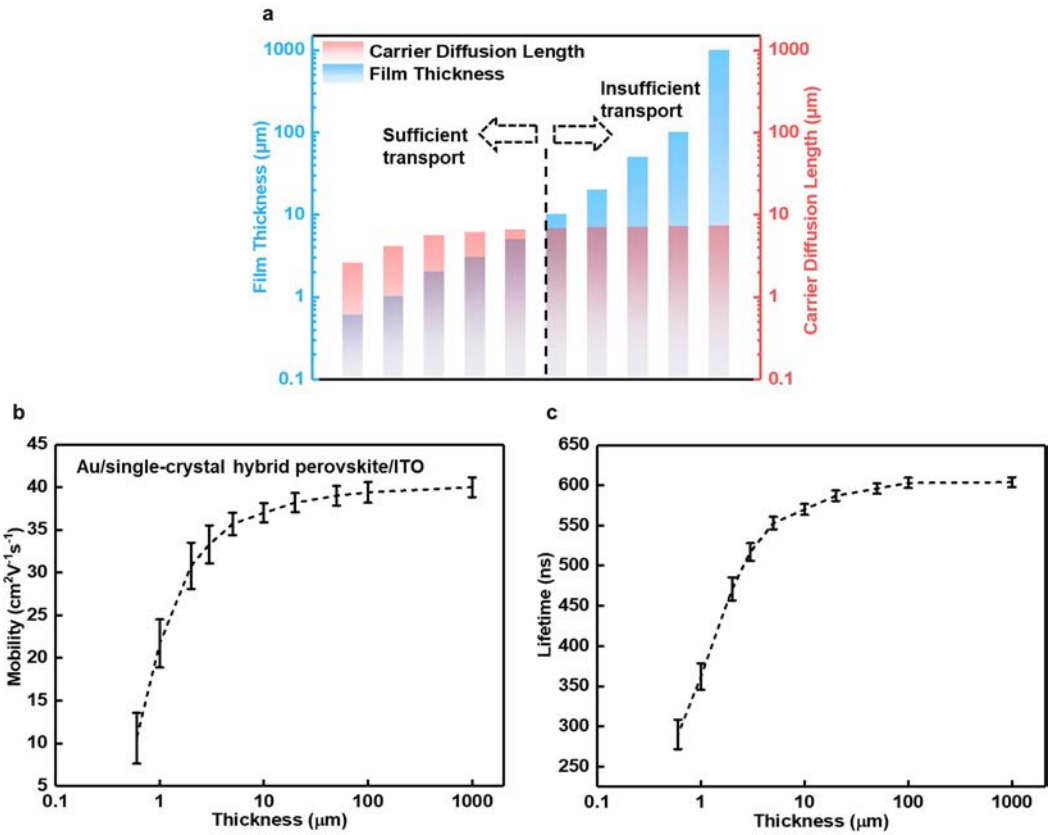

Extended Data Fig. 4 | Carrier diffusion length calculations. a–**c**, Carrier diffusion lengths (**a**) calculated from measured carrier mobilities (**b**) and carrier lifetimes (**c**) with different thicknesses of the single-crystal perovskite. Insufficient charge collection begins when the thickness goes beyond about 5 μm, which can result in a high recombination possibility in the absorber and thus a low device efficiency. Error bars come from three different measurements under the same condition.

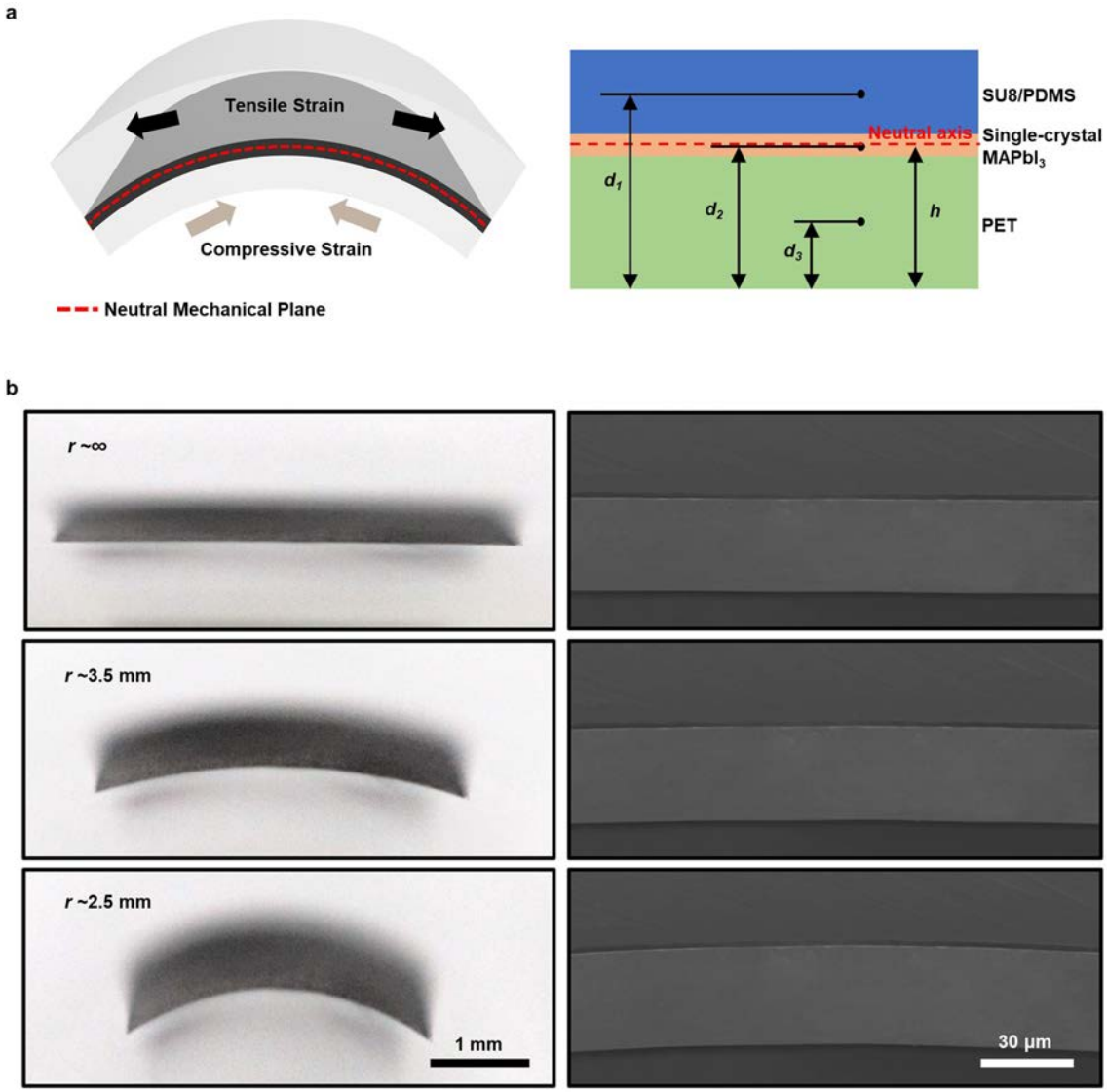

Extended Data Fig. 5 | The NMP design. a, Schematics for calculating the position of the NMP. The SU-8/PDMS top layer is critical for minimizing the strain in the single-crystal perovskite layer. **b**, Optical (left) and SEM (right) images under different bending conditions. The single-crystal perovskite (about 2 μm thick) can be successfully bent to $r \approx 2.5$ mm. All optical images share the same scale bar. All SEM images share the same scale bar.

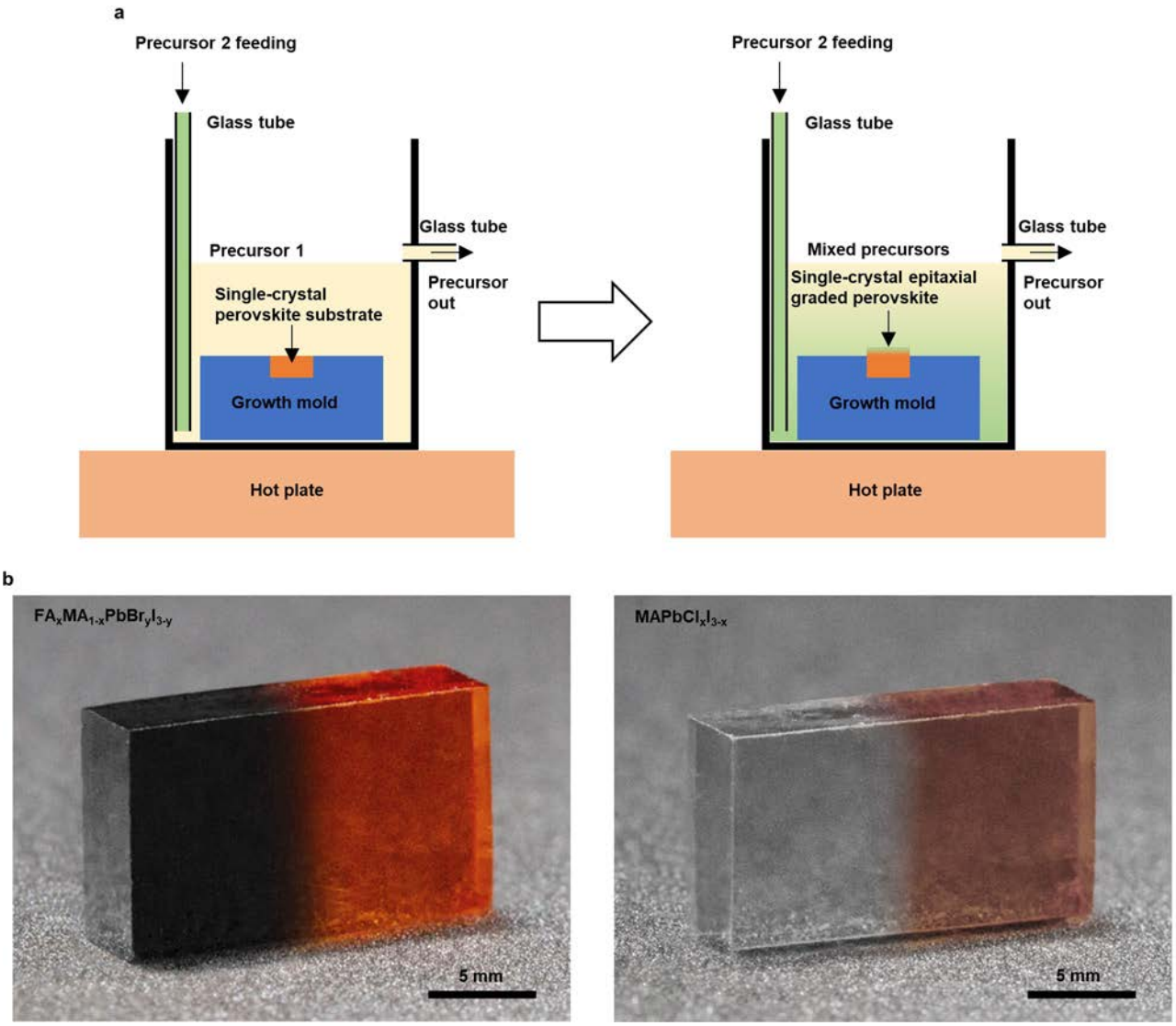

Extended Data Fig. 6 | The growth setup for the bandgap-graded single-crystal perovskites. a, Schematic growth processes with continuously exchanging the precursor solution, which allows the formation of the alloyed structure along the epitaxial growth direction. The perovskite substrate sits in a PDMS growth mould in precursor solution 1. A different precursor solution 2 is fed with designed rates (depending on the solution volume, a calculation example can be seen in Supplementary Discussion 1). **b**, Optical images showing two representative kinds of graded single-crystal perovskites. The alloyed region is at the interface (about 1 mm in width, depending on the alloying rate) between the different coloured crystals. Organic cations, inorganic atoms and halides can all be alloyed.

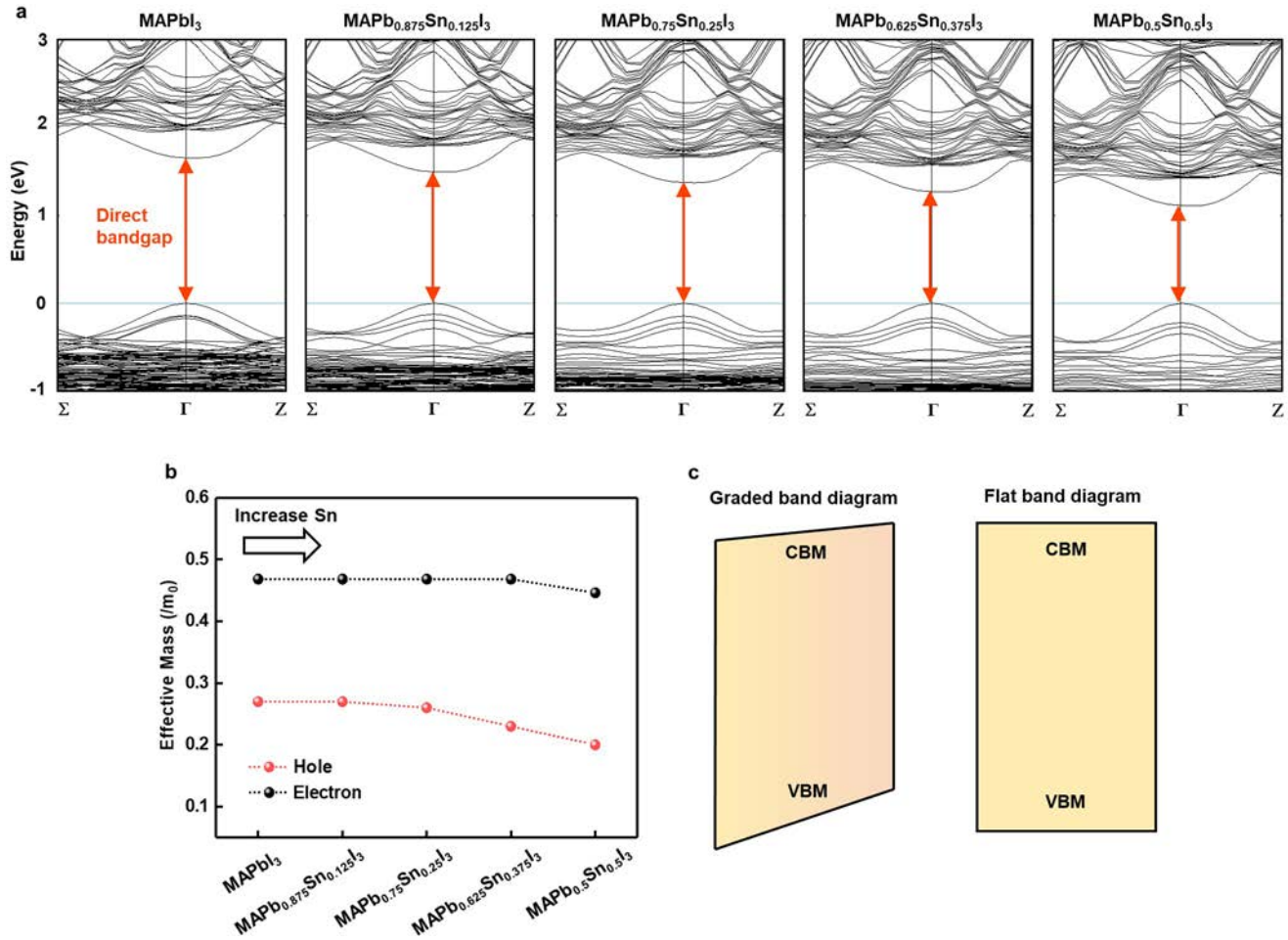

Extended Data Fig. 7 | Density-functional theory simulations of the graded single-crystal perovskites. a, Calculation results showing electronic band structures of the graded single-crystal $MAPb_{0.5+x}Sn_{0.5-x}I_3$. All structures show direct bandgaps at the Γ point. The Fermi level is normalized to the VBM, to show the shrinking tendency of the bandgap. **b**, Calculated effective masses for electrons and holes in the graded single-crystal $MAPb_{0.5+x}Sn_{0.5-x}I_3$ with an increasing tin concentration. The decreasing effective masses indicate increasing mobilities of both electrons and holes. The enhancement for holes is more pronounced than for electrons. **c**, Graded single-crystal $MAPb_{0.5+x}Sn_{0.5-x}I_3$ (left) showing a graded bandgap in comparison with the flat bandgap of conventional $MAPbI_3$ (right).

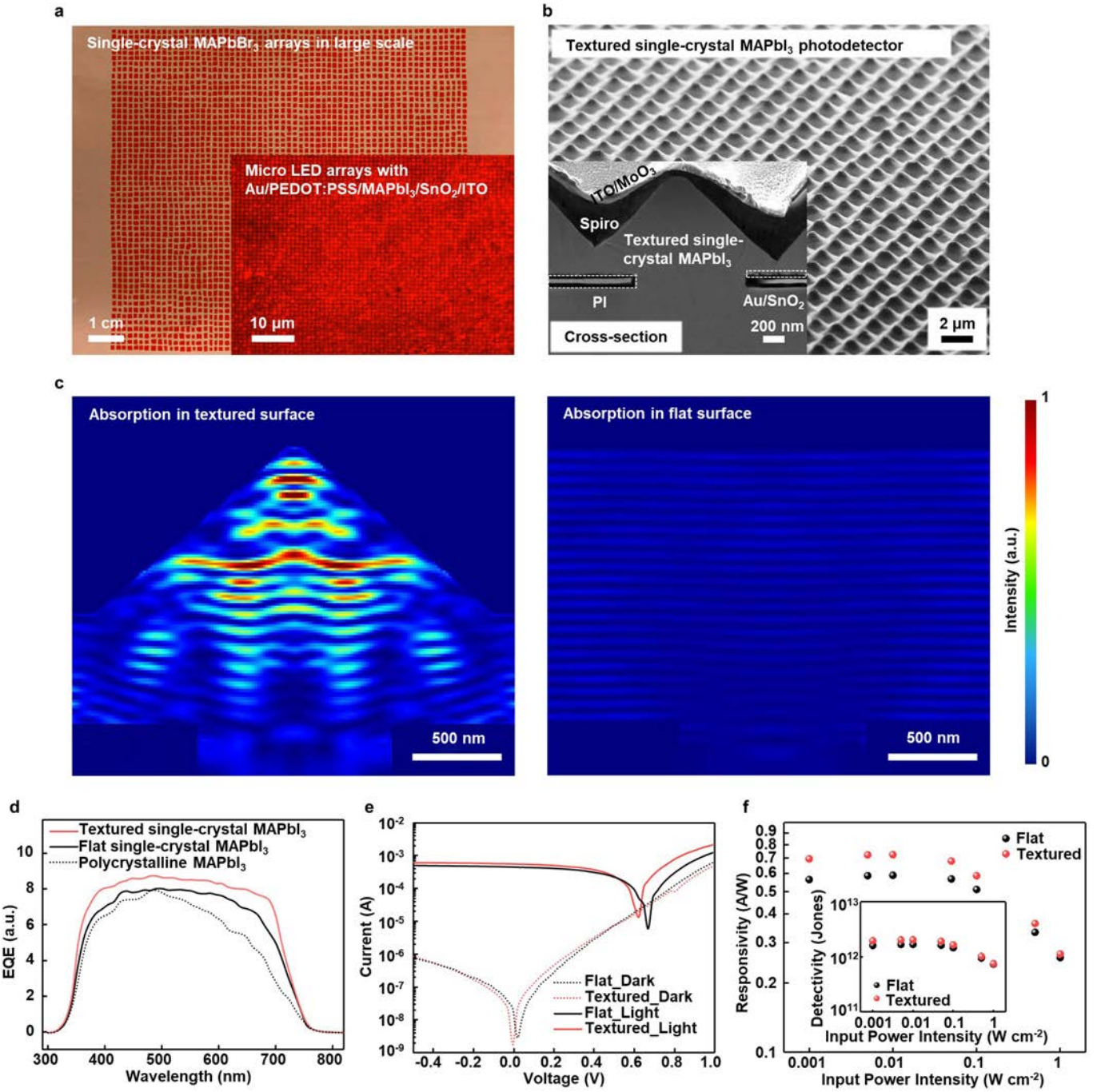

Extended Data Fig. 8 | Single-crystal perovskite thin-film light-emitting diodes and photodetectors fabricated using this growth-and-transfer method. a, Transferred single-crystal $MAPbBr_3$ arrays with each pixel about 100 μm by 100 μm. Inset: the transferred single-crystal $MAPbI_3$ micro light-emitting diode arrays with each pixel about 1 μm by 1 μm. **b**, SEM images showing the textured single-crystal $MAPbI_3$ thin film as a photodetector. Inset: a magnified SEM image of the cross-sectional structure of the device. PI, polyimide. **c**, Finite-difference time-domain optical simulation of the overall absorption by the textured structure (left) and the flat structure (right). The absorption by the textured thin film is much higher than that by the flat one because of the anti-reflective effect. **d**, EQE measurements of different device morphologies. The textured single-crystal film shows the highest quantum efficiency, which comes from the reduced surface reflections. **e**, Dark current measurements on both textured and flat single-crystal devices show that the current levels are similar, indicating the pinhole-free and high-quality thin films. The higher light current of the textured device reveals its higher absorption compared with the flat device. **f**, Responsivity results show that the textured devices are more sensitive to the input power. The inset shows that the textured devices exhibit a higher detectivity than the flat devices. The decreasing tendencies of the responsivity and detectivity at high input power may be due to the material degradation under strong light intensities.

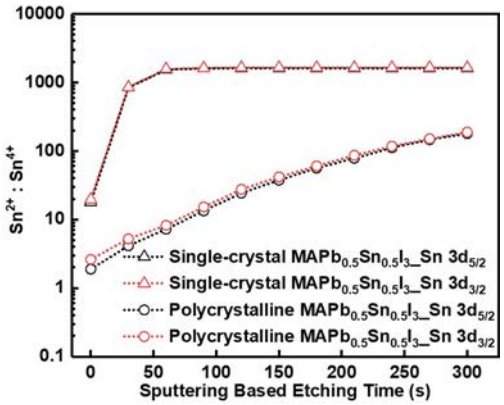

Extended Data Fig. 9 | In situ XPS depth profile studies of different crystal structures. In the single-crystal sample, only the surface areas are easy to be oxidized, indicating that the self-doping in deep areas away from the surface is relatively slow. In the polycrystalline sample, the oxidation is much faster in deep areas compared with the single-crystal samples, indicating that the grain boundaries facilitate the oxidation process.

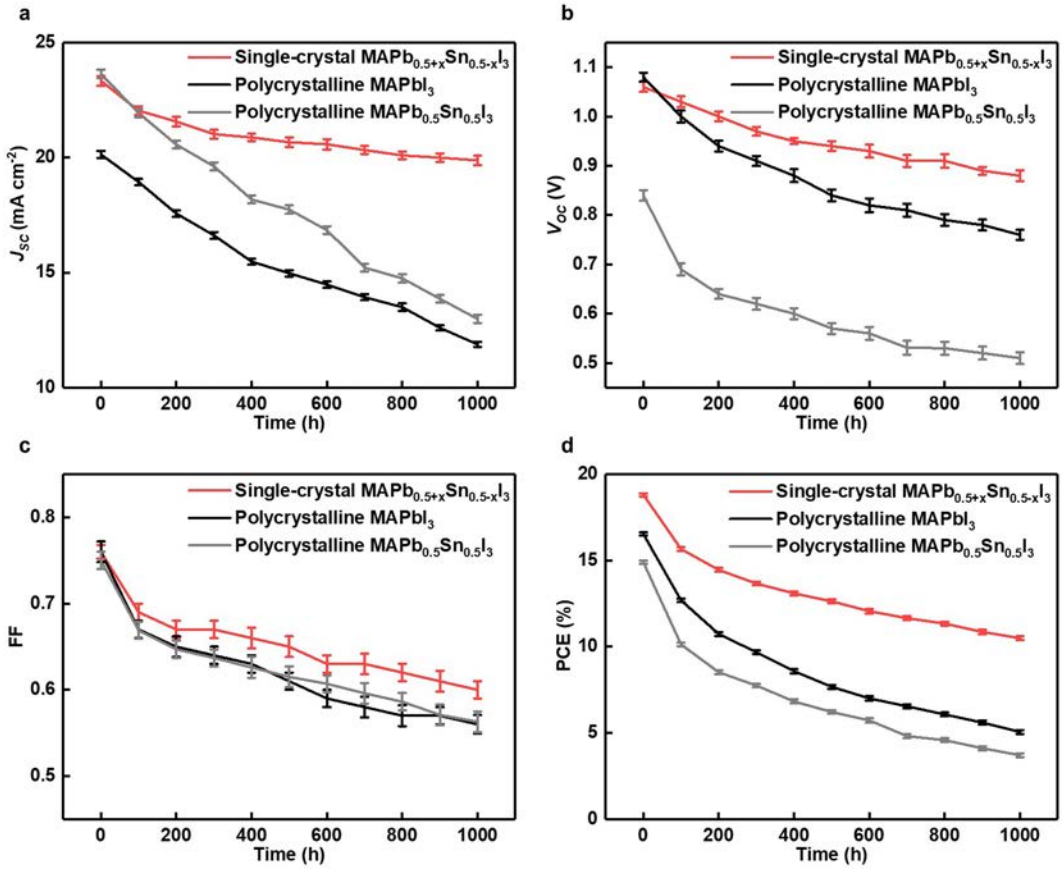

Extended Data Fig. 10 | Long-time continuous illumination stability tests. **a**–**d**, Summarized tracking results of J_{SC} (**a**), V_{OC} (**b**), FF (**c**) and PCE (**d**). The differences between single-crystal and polycrystalline devices are not as large as for the shelf-stability tests in Fig. 4f, which may be because of the poor thermal stability of the hole transport layer (spiro) used in all of these devices. In any case, relatively speaking, single-crystal devices show a better stability than polycrystalline devices.